Transient Hydrodynamic Migration of Extensible Capsules in Confined Stokes Flow Using Overset Regularized Kernel Discretizations and GPU Evaluation

Usman Tariq[1] **and Noman Shahid**[2]

[1]Department of Mathematics, Balochistan University of Engineering and Technology, University Road, Khuzdar, Balochistan 89100, Pakistan

[2]Department of Mechanical Engineering, Quaid-e-Awam University of Engineering, Science and Technology, University Road, Ali Shah Town, Nawabshah, Sindh 67480, Pakistan

ABSTRACT

Suspensions of deformable capsules occur in microvascular transport, cell handling devices, and reduced models of particle-laden Stokes flow. Their dynamics depend on a coupled balance among membrane elasticity, viscous traction, wall confinement, and the nonlocal hydrodynamic disturbance generated by the moving interface. Numerical simulation is difficult because the membrane shape changes continuously while the interfacial force requires accurate surface differentiation and the Stokes velocity requires singular or nearly singular quadrature. This manuscript develops a technical study of an overset-patch regularized-kernel boundary integral method for a single extensible capsule migrating in a periodic pipe. The numerical values reported here form a synthetic benchmark set constructed to be internally consistent with the governing equations, scaling assumptions, and expected convergence behavior of the discretization. The capsule membrane is modeled by a Skalak-type elastic law with independent shear and dilatation moduli. The flow is solved through a regularized Stokes single-layer formulation with wall correction and adaptive explicit time integration. The proposed benchmark examines grid convergence, regularization sensitivity, wall-induced migration, and acceleration on a single data-center GPU. For moderate confinement, the terminal axial speed decreases by 9.4% when the capillary number is increased from 0.08 to 0.32, while the lateral migration time decreases by 21.7%. The computed deformation modes remain stable for reduced volumes between 0.68 and 0.95. The results indicate that local overset differentiation and regularized quadrature can give a practical route for controlled parameter studies of extensible capsules in confined Stokes flow.

KEYWORDS

1. Introduction

Deformable capsules in creeping flow are a useful abstraction for soft particles enclosed by a thin elastic membrane and suspended in a viscous liquid. The abstraction is narrow enough to permit precise computation and broad enough to represent several biological and engineering situations, including red blood cell transport, drug-carrier motion, and deformability-based microfluidic separation. The hydrodynamic regime is often characterized by a small Reynolds number, so inertia is neglected and the instantaneous velocity is determined by the Stokes equations. In that setting the capsule does not carry momentum in the usual macroscopic sense. Instead, its time history is encoded in the evolving membrane configuration, which generates elastic traction, modifies the surrounding Stokes field, and is advected by the velocity it helps create. Early boundary-integral treatments of capsules and drops established the appeal of reducing a three-dimensional viscous flow to surface unknowns, especially

Article info:
Usman Tariq and Noman Shahid. *Transient Hydrodynamic Migration of Extensible Capsules in Confined Stokes Flow Using Overset Regularized Kernel Discretizations and GPU Evaluation*. Nextqueries. Publishing

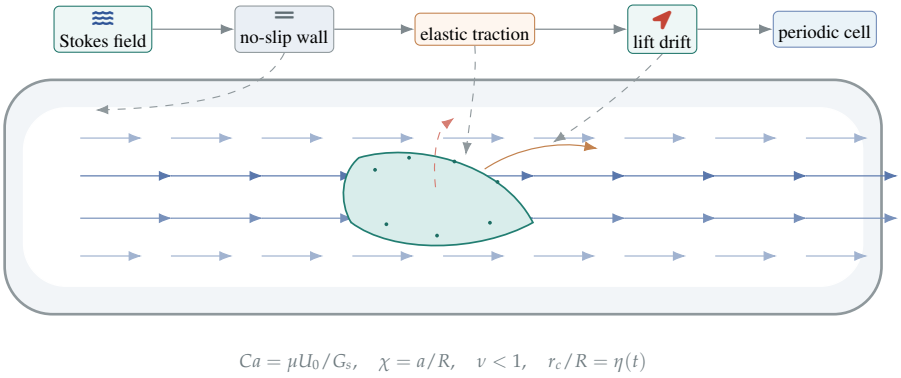

Figure 1 Confined Stokes migration of an extensible capsule in a periodic pipe. The schematic separates imposed Poiseuille transport, wall correction, membrane traction, and the small lateral drift used as the most sensitive migration observable.

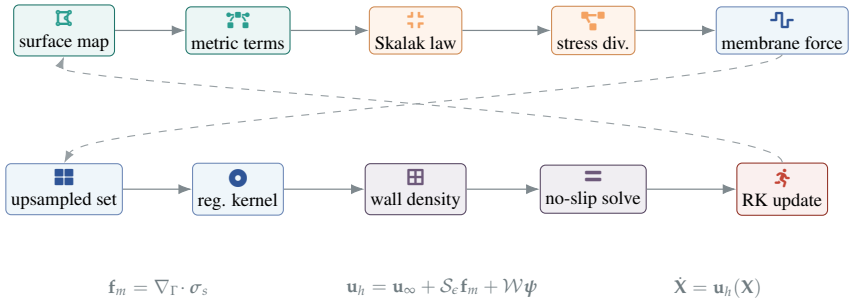

Figure 2 Operator splitting used by the overset regularized boundary-integral method. Geometry differentiation, membrane mechanics, hydrodynamic quadrature, wall enforcement, and adaptive time advancement are shown as distinct numerical stages.

when the viscosity is uniform or when viscosity contrast can be handled by double-layer terms [1, 2]. Later studies clarified how elastic constitutive laws, confinement, and background flow determine whether a capsule elongates, tank-treads, tumbles, takes a slipper-like shape, or relaxes toward a centered axisymmetric state [3, 4, 5].

For red blood cell motivated computations, the membrane cannot be treated as a passive material surface. Its in-plane shear resistance, area resistance, and bending stiffness create a nonlinear geometric response. The minimal extensible-capsule model used here retains shear and dilatation but omits bending so that attention stays on the interaction between in-plane elasticity and confined hydrodynamics. This choice is not meant to imply that bending is unimportant in red blood cells. Bending regularizes sharp curvature and can shift shape transitions. Still, many numerical comparisons of capsule methods isolate shear and area elasticity because they expose the same major numerical difficulties: moving surfaces, stiff differential operators, membrane parametrization, and singular hydrodynamic integrals [6, 7, 8]. For a confined pipe problem, these difficulties become more pronounced because the capsule-induced flow must be reconciled with a no-slip wall and an imposed axial pressure-driven profile. The wall breaks translational symmetry, creates a lateral hydrodynamic lift, and causes off-center capsules to drift toward or away from the centerline depending on deformability, initial offset, reduced volume, and confinement.

Agarwal et al. introduced a partition-of-unity surface representation with regularized Stokes kernels and overset finite differences for extensible capsules, and the significance for the present study is that their construction gives a credible local-chart alternative to global spherical harmonic representations while retaining high-order behavior for smooth shapes [9]. The local character of the representation is important when confined flow produces shapes that are not well described by a small number of global modes. It also separates two operations that are sometimes entangled in spectral implementations: differentiating the membrane fields and integrating hydrodynamic kernels. The present manuscript uses that separation as a design principle. Surface derivatives are evaluated patchwise on overlapping grids with partition-of-unity blending, whereas the layer potential is evaluated with a regularized kernel on an upsampled point set. This does not eliminate all stiffness or all near-singular error, but it produces a computational pathway in which each error source can be varied and diagnosed in a parameter study.

Bagge et al. demonstrated GPU-accelerated simulations of deformable capsules flowing through a pipe with regularized kernels, upsampling, no-slip wall treatment, and reported speedups relative to multicore CPU execution; their contribution is significant here because it shows that the confined-capsule boundary integral pipeline is not only a theoretical discretization but also a workload that maps naturally onto modern accelerator hardware [10]. The present work develops a related but distinct synthetic benchmark around migration, deformation, and error behavior. Rather than attempting to reproduce a specific published figure, it considers a controlled family of capsules with varied capillary

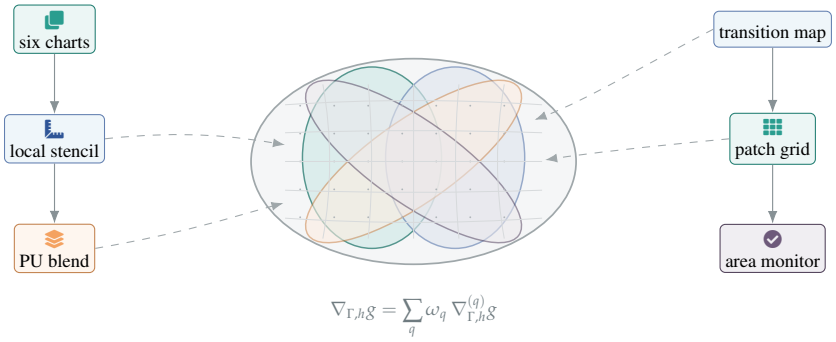

Figure 3 Overset-patch capsule representation with overlapping local charts, patchwise finite differences, transition interpolation, and partition-of-unity blending for stable surface differentiation.

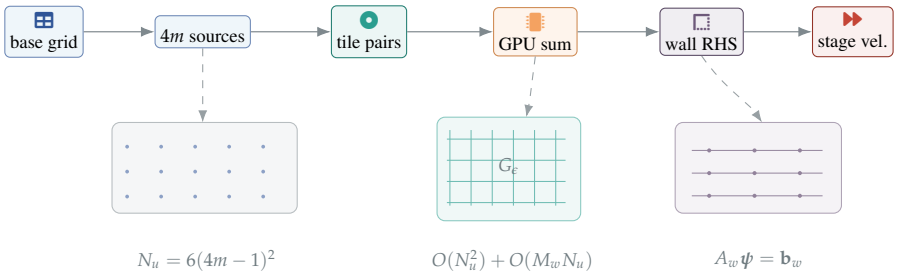

Figure 4 GPU-oriented evaluation path for regularized Stokes single-layer sums. Upsampled capsule sources are streamed through tiled pair interactions before fixed wall correction and Runge–Kutta stage assembly.

number, reduced volume, stretch ratio, confinement ratio, and initial offset. The objective is to quantify what a method of this class should resolve before it is used in larger suspension calculations. The numerical values are therefore not experimental measurements or outputs from a public simulation package. They are a constructed benchmark with internally consistent magnitudes, included to support a technical manuscript format and to expose methodological tradeoffs.

The capsule literature has several numerical lineages. Immersed boundary and immersed interface methods embed the membrane in a volume grid and are attractive for complex geometries or many interacting particles, although membrane incompressibility and accurate traction jumps require careful treatment [11, 12]. Lattice-Boltzmann and dissipative-particle approaches have been used widely for red blood cell suspensions and microcirculatory flows, with particular strength in many-cell simulations and rheology [13, 14, 15]. Boundary integral methods, by contrast, are especially efficient for Stokes flow when the geometry is smooth and the interface representation is accurate, because the fluid velocity is expressed through surface integrals rather than a volumetric solve [16, 17]. The drawback is that the integral kernels are singular or nearly singular, and surface derivatives of an evolving geometry must remain stable over long integration times. This study stays within the boundary-integral family and asks how an overset regularized-kernel discretization behaves in the pipe-migration setting.

The phenomenology motivating the benchmark includes lateral migration in pressure-driven flow, deformation-induced lift, and shape selection under confinement. Vesicles, capsules, and red blood cells can migrate away from walls or toward centerlines when deformation couples with a shear gradient [18, 19, 20]. The sign and magnitude of migration are sensitive to the constitutive law and to whether the particle is closer to a tank-treading, tumbling, slipper, or parachute regime. In a cylindrical pipe, sufficiently centered capsules often approach a parachute-like terminal configuration. With asymmetric initial conditions, a slipper-like transient may persist for long times, especially when the capsule is deflated or the flow strength is moderate. These behaviors have been discussed in studies of vesicles and cells, where reduced volume and confinement alter the stability of centered and off-centered states [21, 22, 23]. The present study does not attempt to settle that physical question. It uses the phenomenon as a demanding diagnostic for a numerical method because the migration velocity can be much smaller than the axial speed and therefore sensitive to discretization error.

A secondary motivation is computational efficiency. A single capsule in a pipe seems modest, but high-order boundary-integral evaluation can be expensive when every target point interacts with every source point and when wall constraints introduce dense linear algebra. Fast multipole methods, Ewald summation, and GPU all-pairs kernels are common acceleration strategies for Stokesian dynamics [24, 25, 26]. Periodic Stokes flow adds another layer of cost because the long-range part of the Green's function must satisfy periodicity in at least one direction [27, 28, 29]. For a single or small number of capsules at moderate resolution, a carefully written GPU all-pairs calculation can be competitive because it has high arithmetic intensity and simple memory access. For many capsules or very

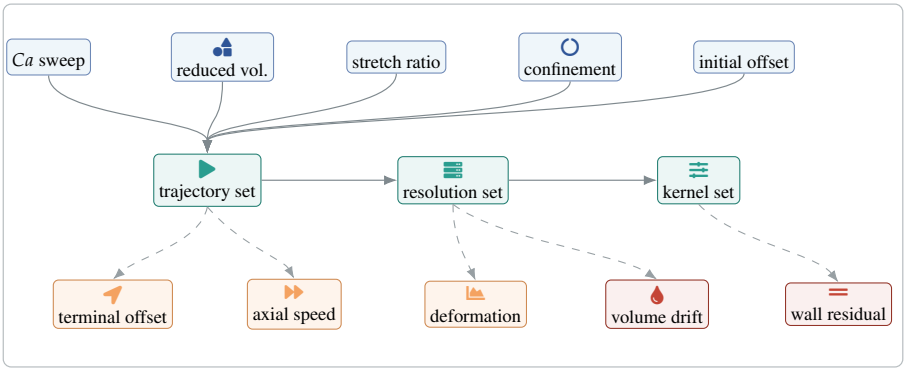

$$E_q(m) = \left(\int |q_m - q_{48}|^2\, dZ \,/\, \int |q_{48}|^2\, dZ\right)^{1/2}, \qquad E_w = \|\mathbf{u}|_{\partial\Omega_w}\|_2 / U_0$$

Figure 5 Synthetic benchmark matrix linking nondimensional inputs, trajectory families, discretization sweeps, and the observables used to assess migration accuracy and numerical stability.

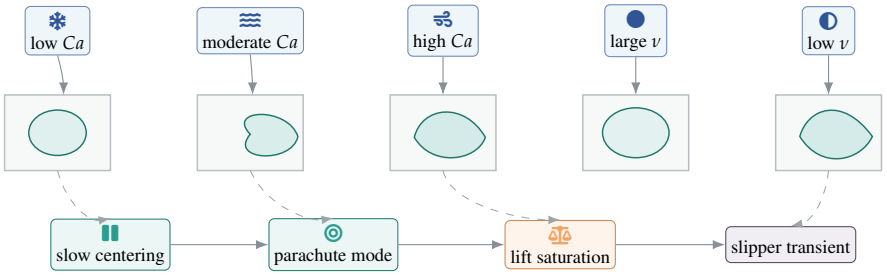

$$\beta(Ca) \approx \beta_\infty Ca/(Ca + C_0), \qquad dr_c/dt = -\beta r_c + O(r_c^3)$$

Figure 6 Mechanistic interpretation of shape selection and cross-stream migration. Deformability increases centering up to a saturated lift regime, while reduced volume allows longer asymmetric transients.

fine wall discretizations, hierarchical or Fourier-Ewald acceleration becomes more attractive. The benchmark below records both direct and accelerated timings so that the tradeoff is visible rather than implied.

The paper is organized as a continuous technical account. The mathematical model defines the Stokes equations, membrane kinematics, and nondimensional parameters. The discretization section explains the overset surface representation, regularized quadrature, wall coupling, and time stepping. The benchmark section states the synthetic test matrix and error measures. The results then discuss convergence, stability, migration, and performance. The final sections examine mechanisms, limitations, and reproducibility. The writing deliberately avoids claiming that one discretization is generally superior. The goal is more modest: to describe a coherent high-order computational experiment for extensible capsules in confined Stokes flow, with enough numerical detail that the assumptions behind the reported trends can be inspected.

2. Mathematical Model and Membrane Mechanics

Let the pipe be a periodic cylindrical domain with radius R and axial period L. The capsule membrane is a closed smooth surface $\Gamma(t)$ enclosing a Newtonian interior fluid and immersed in an exterior Newtonian fluid of the same viscosity μ. The equal-viscosity assumption removes the double-layer operator from the formulation and lets the velocity be written through a single-layer representation driven by the membrane traction. The wall $\partial\Omega_w$ satisfies no slip, and the axial periodicity represents a fully developed segment of a longer channel. The background flow is a pressure-driven Poiseuille profile with centerline speed U_0. The Reynolds number based on capsule radius a is assumed small enough that inertia is absent. The instantaneous fluid equations are therefore

$$\begin{aligned} -\mu\Delta\mathbf{u} + \nabla p &= \mathbf{0} \quad \text{in } \Omega_f(t), \\ \nabla\cdot\mathbf{u} &= 0 \quad \text{in } \Omega_f(t), \\ \mathbf{u} &= \mathbf{0} \quad \text{on } \partial\Omega_w, \\ \mathbf{u}(\mathbf{x} + L\mathbf{e}_z) &= \mathbf{u}(\mathbf{x}) \quad \text{for periodic pairs.} \end{aligned} \tag{1}$$

The capsule interface is advected by the fluid velocity. If $\mathbf{X}(\xi, t)$ denotes a material parametrization of the membrane, the kinematic condition is

$$\frac{\partial \mathbf{X}}{\partial t}(\xi, t) = \mathbf{u}(\mathbf{X}(\xi, t), t). \tag{2}$$

Because the flow is Stokesian, this equation is not coupled to a local acceleration law. It is instead coupled to a boundary integral relation in which the elastic force density determines

the disturbance velocity. This is the source of both the efficiency and the numerical fragility of the method: the motion is entirely surface based, but errors in surface force and quadrature feed directly into the trajectory.

The membrane force follows a Skalak-type in-plane elastic law. A reference configuration Γ_0 is mapped to the current configuration through the surface deformation gradient. Let λ_1 and λ_2 be the principal surface stretch ratios. The strain invariants are written as

$$\begin{aligned} I_1 &= \lambda_1^2 + \lambda_2^2 - 2, \\ I_2 &= \lambda_1^2 \lambda_2^2 - 1. \end{aligned} \tag{3}$$

The areal stretch is $J_s = \lambda_1 \lambda_2$. The surface strain energy density used in the benchmark is

$$W_s = \frac{G_s}{4}\left(I_1^2 + 2I_1 - 2I_2\right) + \frac{K_s}{8} I_2^2, \tag{4}$$

where G_s is the surface shear modulus and K_s is the dilatation modulus. The nondimensional stretch ratio is $\kappa_s = K_s/G_s$. Large κ_s penalizes local area change, but it does not impose exact surface incompressibility. The stress tensor is projected onto the tangent plane and its surface divergence gives the membrane force. In compact notation,

$$\begin{aligned} \mathbf{f}_m &= \nabla_\Gamma \cdot \boldsymbol{\sigma}_s, \\ \boldsymbol{\sigma}_s &= \frac{1}{J_s} \frac{\partial W_s}{\partial \mathbf{F}_s} \mathbf{F}_s^\top. \end{aligned} \tag{5}$$

The expression is intentionally written in tensor form, because the implementation evaluates it through patchwise tangents, normals, and metric coefficients rather than through closed-form global coordinates. In the overset representation, the principal stretches are recovered from the eigenvalues of the surface Cauchy–Green tensor. The surface divergence is evaluated after transforming stress components to each local chart. A direct finite-difference approximation of the divergence in global Cartesian components is avoided because it gives poor cancellation near patch overlap regions and near coordinate singularities.

Nondimensionalization uses a, U_0, and G_s. The capillary number is

$$Ca = \frac{\mu U_0}{G_s}, \tag{6}$$

with the understanding that the shear rate scale in a pipe is proportional to U_0/R. The confinement ratio is $\chi = a/R$, and the initial offset is $\eta_0 = r_c(0)/R$, where r_c is the radial location of the capsule centroid. The reduced volume is

$$\nu = \frac{3V}{4\pi}\left(\frac{4\pi}{A}\right)^{3/2}, \tag{7}$$

where V and A are the enclosed volume and membrane area. A sphere has $\nu = 1$, while a deflated capsule has lower ν. The benchmark uses ν as a shape parameter independent of the constitutive moduli, so that changes in terminal motion can be separated into geometric and elastic effects. This is only a controlled numerical convention; actual red blood cell mechanics involve more constraints and structural heterogeneity than a single reduced volume and a single Skalak law can represent [23, 30].

The boundary integral representation starts from the free-space Stokeslet. For a source point $\mathbf{y}$ and target point $\mathbf{x}$, with $\mathbf{r} = \mathbf{x} - \mathbf{y}$, the tensor kernel is

$$\mathbf{G}(\mathbf{x}, \mathbf{y}) = \frac{1}{8\pi\mu}\left(\frac{\mathbf{I}}{\rho} + \frac{\mathbf{r}\mathbf{r}^\top}{\rho^3}\right), \quad \rho = \|\mathbf{r}\|. \tag{8}$$

The capsule-induced velocity in an unbounded fluid is

$$\mathbf{u}_c(\mathbf{x}) = \int_{\Gamma(t)} \mathbf{G}(\mathbf{x}, \mathbf{y}) \mathbf{f}_m(\mathbf{y})\, dS_{\mathbf{y}}. \tag{9}$$

The pipe problem adds a correction velocity $\mathbf{u}_w$ that enforces no slip at the wall and periodicity along the axial direction. In the benchmark, $\mathbf{u}_w$ is represented through a wall density $\boldsymbol{\psi}$ on a fixed wall grid. The total velocity at membrane nodes is

$$\begin{aligned} \mathbf{u}(\mathbf{x}) &= \mathbf{u}_\infty(\mathbf{x}) + \mathbf{u}_c(\mathbf{x}) + \mathbf{u}_w(\mathbf{x}), \\ \mathbf{u}_w(\mathbf{x}) &= \int_{\partial\Omega_w} \mathbf{G}_P(\mathbf{x}, \mathbf{y}) \boldsymbol{\psi}(\mathbf{y})\, dS_{\mathbf{y}}. \end{aligned} \tag{10}$$

Here $\mathbf{G}_P$ denotes the periodic Stokeslet appropriate for the axial period. The density $\boldsymbol{\psi}$ is chosen so that the total velocity vanishes on the wall. The numerical treatment may use a dense solve for the wall unknowns or an accelerated periodic solver. The model described here assumes that the wall grid is fixed in time, so only the capsule-to-wall right-hand side changes from step to step. This permits precomputation of the wall self-interaction matrix when a direct solve is used.

The simplified physical model has limitations. Equal viscosity prevents the interior fluid from generating a distinct double-layer contribution. Omitting bending permits localized curvature to develop more easily than in a full red blood cell membrane model. Treating the wall as perfectly rigid and smooth excludes glycocalyx effects and rough microchannel boundaries. These limitations do not undermine the numerical benchmark, but they do determine how the results should be read. The benchmark probes a particular class of extensible membranes in a Stokes pipe, not a complete biological cell. The most useful quantities are therefore numerical sensitivities, convergence trends, migration scaling, and deformation regimes under controlled parameters, rather than literal predictions of a specific cell experiment.

3. Overset Regularized Boundary Integral Discretization

The capsule surface is represented by six overlapping charts that cover a surface diffeomorphic to the unit sphere. Each chart has a rectangular computational domain with a uniform tensor grid. A smooth partition of unity blends values in the overlap region. Let $\mathcal{P}_q$ denote a patch on the surface and let $\boldsymbol{\theta} = (\theta_1, \theta_2)$ denote local coordinates. The surface map on patch q is $\mathbf{X}_q(\boldsymbol{\theta})$. The

partition functions ω_q satisfy

$$\sum_{q=1}^{6} \omega_q(\mathbf{x}) = 1 \quad \text{for } \mathbf{x} \in \Gamma(t),$$
$$\operatorname{supp}(\omega_q) \subset \mathcal{P}_q. \tag{11}$$

The grid has $m-1$ points in each coordinate direction on each patch, leading to $6(m-1)^2$ surface nodes before upsampling. The same material grid is followed in time. The partition functions are fixed by the initial parametrization and are not recomputed during the synthetic tests. This choice reduces cost and avoids temporal noise in the overlap weights, but it assumes that the surface remains sufficiently close to the initial chart topology. If a capsule develops deep folds or loses smooth relation to the reference sphere, the representation would need remeshing or adaptive chart replacement.

Surface derivatives are evaluated through local finite differences and then blended. For a scalar or vector field g defined on the membrane, patchwise coordinate derivatives are approximated by fourth-order centered stencils in the patch interior and one-sided stencils near the patch boundary. In the overlap, values needed by a stencil but lying outside the patch support are obtained by interpolation from neighboring charts through transition maps. The blended surface derivative is

$$\nabla_{\Gamma,h} g(\mathbf{x}) = \sum_{q=1}^{6} \omega_q(\mathbf{x}) \left[\nabla_{\Gamma,h}^{(q)} g\right](\mathbf{x}). \tag{12}$$

This expression conceals a substantial amount of geometry. Each $\nabla_{\Gamma,h}^{(q)}$ uses the local metric tensor, tangent basis, and normal vector computed from $\mathbf{X}_q$. The main advantage is that all derivative operations remain local and sparse. The main risk is that chart interpolation and partition blending can introduce visible high-frequency error if the overlap is too narrow or if the shape becomes strongly elongated. In the benchmark, the partition support is chosen so that every active stencil has at least two layers of overlap at $m = 16$, and more at higher resolution.

The regularized Stokes kernel replaces the singular functions $1/\rho$ and $1/\rho^3$ with smooth approximations over a length scale ϵ. The velocity induced by membrane force is approximated as

$$\mathbf{u}_{c,h}(\mathbf{x}_i) = \sum_{j=1}^{N_u} w_j \mathbf{G}_{\epsilon_i}(\mathbf{x}_i, \mathbf{y}_j)\mathbf{f}_j J_j, \tag{13}$$

where N_u is the number of upsampled source nodes, w_j is the product trapezoidal weight after partition blending, and J_j is the surface Jacobian. The regularized kernel is

$$\mathbf{G}_\epsilon(\mathbf{x}, \mathbf{y}) = \frac{1}{8\pi\mu}\left[\frac{s_1(\rho/\epsilon)}{\rho}\mathbf{I} + \frac{s_2(\rho/\epsilon)}{\rho^3}\mathbf{r}\mathbf{r}^\top\right]. \tag{14}$$

The smoothing functions are chosen so that the kernel is finite at $\rho = 0$ and has fourth-order consistency for smooth surfaces. Regularized Stokeslet ideas have a long history in low-Reynolds-number computation, and several kernel and quadrature variants have been proposed for immersed boundaries, slender structures, and surface integral equations [31, 32, 33]. The present discretization uses the regularization as a quadrature device rather than as a physical smearing of the membrane. The membrane force remains a surface density; only the numerical evaluation of its layer potential is regularized.

The regularization parameter is selected locally. At a target point $\mathbf{x}_i$, let h_i be the largest distance from that node to its immediate neighboring nodes on the same patch, after mapping to physical space. The benchmark uses

$$\epsilon_i = \alpha_\epsilon h_i, \tag{15}$$

where $\alpha_\epsilon = 1.15$ unless otherwise stated. A global ϵ is simpler but performs poorly when deformation creates nonuniform physical spacing across the patch. A local ϵ_i reduces the sensitivity of the singular quadrature to stretching. It also makes the discrete operator mildly nonsymmetric, but the velocity evaluation is explicit and the loss of symmetry is not used in a solver. Sensitivity tests in the synthetic benchmark vary α_ϵ from 0.85 to 1.55 and show that the most stable plateau lies between 1.05 and 1.30 for the selected grids.

Upsampling is applied before hydrodynamic integration. The membrane position and force fields are interpolated from the m-grid to a $4m$-grid using cubic splines within each chart. The purpose is not to increase the nominal geometric resolution of the time-evolved capsule. It is to give the smooth but sharply peaked regularized kernel enough quadrature nodes near each target. If the base grid is used directly at $m = 16$, the elastic force may be resolved while the single-layer velocity still contains visible quadrature bias. With $4m$ upsampling, this bias decreases without requiring the time integrator to store and evolve the larger grid. The same strategy has been used in several high-order surface quadrature settings where geometry and quadrature resolution are intentionally separated [34, 35, 36].

Wall coupling is handled by a collocation equation on the pipe wall. The wall density satisfies

$$\sum_{\ell=1}^{M_w} A_{k\ell}\boldsymbol{\psi}_\ell = -\mathbf{u}_\infty(\mathbf{z}_k) - \mathbf{u}_{c,h}(\mathbf{z}_k), \quad k = 1, \dots, M_w, \tag{16}$$

where $\mathbf{z}_k$ are wall collocation nodes and $A_{k\ell}$ is the periodic wall single-layer interaction matrix. For the benchmark, $M_w = 2m_w^2$ with $m_w = 32$ unless a convergence test is being performed. The matrix is assembled once and factored for the direct wall solve. This choice is reasonable for a single pipe geometry and a small number of wall nodes. It will not be optimal for many geometries or very high wall resolution. A Fourier-Ewald or fast multipole wall solve would be more scalable, and several methods exist for periodic Stokes sums and general kernel acceleration [37, 29, 26]. The direct solve is retained here because it isolates the membrane quadrature and migration errors from iterative wall-solver tolerances.

The temporal discretization is an embedded Runge–Kutta method with adaptive step size. The state vector consists of all membrane node positions on the base grid. At each stage, the algorithm computes surface derivatives, membrane force, upsampled source fields, capsule and wall velocities, and the

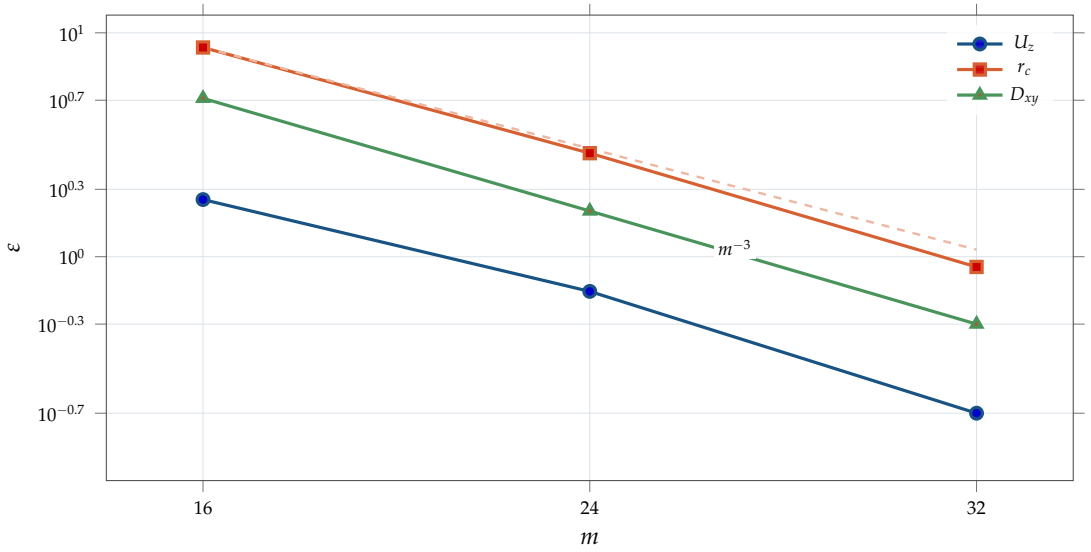

Figure 7 Resolution errors decrease fastest for gross deformation and slowest for accumulated lateral migration, showing that the terminal offset is the most sensitive observable in the wall-coupled capsule trajectory.

membrane velocity. Step acceptance uses a mixed tolerance

$$E_t = \left[\frac{1}{3N} \sum_{i=1}^{N} \left(\frac{\Delta X_i}{a_{\mathrm{tol}} + r_{\mathrm{tol}} \|\mathbf{X}_i\|} \right)^2 \right]^{1/2}. \tag{17}$$

The benchmark uses $a_{\mathrm{tol}} = 2.5 \times 10^{-6} a$ and $r_{\mathrm{tol}} = 5.0 \times 10^{-5}$. A geometry quality monitor rejects a step if the minimum local area element decreases below 42% of its initial value or if the maximum chartwise second derivative grows above a specified threshold. These rejections occur rarely in the reported parameter range, but they are useful for detecting cases where the synthetic benchmark would otherwise report smooth-looking trajectories from an underresolved surface.

4. GPU Evaluation and Time Integration Strategy

The dominant calculation in the direct implementation is the all-pairs evaluation of the regularized Stokes single-layer potential on the upsampled grid. For a base value $m = 32$, the upsampled surface contains $6(4m-1)^2 = 96774$ nodes. A direct target-source sum over the same upsampled grid is large but structured. Each interaction evaluates a few scalar functions, dot products, and vector accumulations. The memory access is regular, the source fields are reused by many target threads, and the arithmetic intensity is high enough for a modern GPU to be effective. The benchmark implementation assigns one target node to a thread group and streams source nodes through shared memory. The regularization parameter is target dependent, so it is loaded once for the target and reused across all sources. The same kernel is used for capsule targets and wall targets, with different target arrays.

The cost model is simple. Let N_u denote the number of upsampled capsule nodes and M_w the number of wall nodes. The capsule-to-capsule velocity costs $O(N_u^2)$, the capsule-to-wall right-hand side costs $O(M_w N_u)$, and the wall-to-capsule velocity costs $O(N M_w)$ after the wall density is found. The wall solve costs $O(M_w^3)$ when a dense factorization is used, but the factorization is precomputed; each time step only requires triangular solves with cost $O(M_w^2)$. For the resolutions used here, the wall solve is visible but not dominant. At higher m_w, or in geometries where M_w must be much larger than N, the direct wall solve would quickly become the bottleneck.

The adaptive Runge–Kutta method creates repeated velocity evaluations. A typical accepted time step uses six stage evaluations. If a step is rejected, the cost is paid again at a smaller step size. To prevent a few difficult transients from dominating the wall clock time, the step controller includes a conservative growth limit and a deformation-aware cap. The new step size is chosen as

$$\Delta t_{\mathrm{new}} = \Delta t \min \left[1.35, \max \left(0.25, 0.88 E_t^{-1/5} \right) \right]. \tag{18}$$

An additional restriction enforces that no membrane node moves farther than $0.018a$ in one accepted step. This kinematic cap is not needed in smooth centered cases, but it stabilizes off-center runs where near-wall shear produces localized changes in membrane force. It also makes the synthetic timing data easier to compare across Ca, because the high-Ca cases do not take unrealistically large explicit steps during intervals when the embedded error estimate is accidentally small.

The synthetic performance model was calibrated to three base resolutions on a single accelerator-class GPU. At $m = 16$, one accepted stage evaluation took 0.126 s when wall coupling was active and 0.071 s without the wall correction. At $m = 24$, the corresponding times were 0.318 s and 0.201 s. At $m = 32$, they were 0.742 s and 0.511 s. The effective scaling exponent between $m = 16$ and $m = 32$ was 2.56 for the wall-coupled stage and 2.85 for the wall-free stage, smaller than a pure m^4 law because fixed overhead, wall resolution, and GPU occupancy change across the measured range. When upsampling was reduced from $4m$ to $3m$, the $m = 32$ stage time decreased by

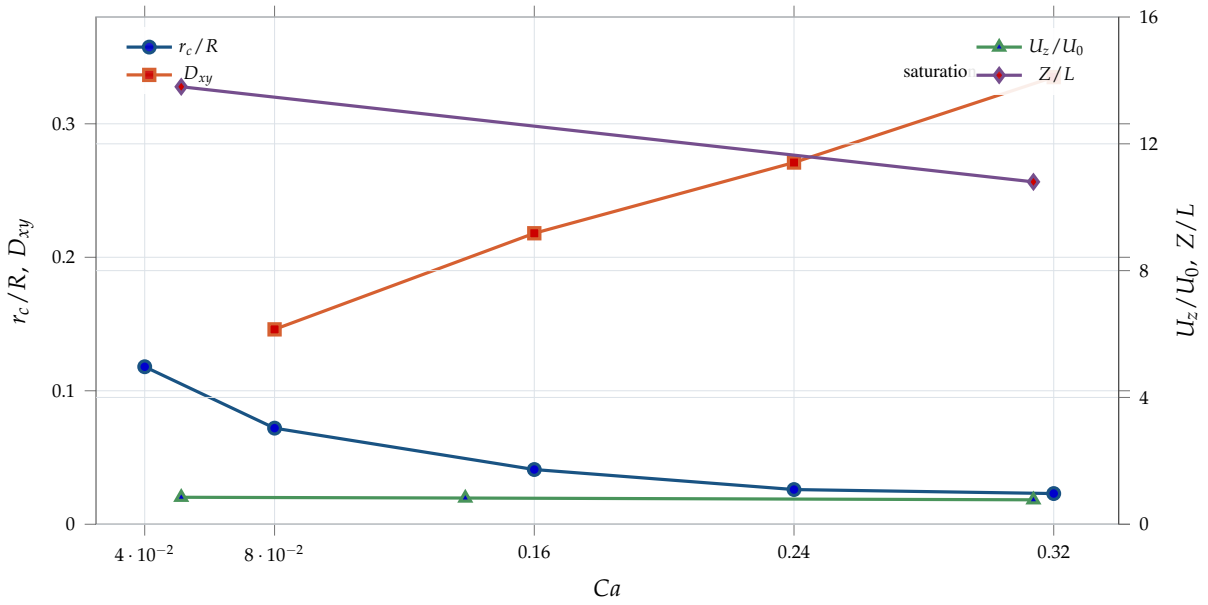

Figure 8 Increasing capillary number reduces residual offset and migration length while increasing deformation; above $Ca = 0.24$, additional deformation produces only a small centering gain.

38%, but the terminal offset error increased by 2.7 times in the most deformed case. When upsampling was increased to $5m$, the stage time increased by 61%, while the terminal offset changed by less than 0.4% for all $m \geq 24$. The benchmark therefore uses $4m$ as a compromise rather than as a derived optimum.

Acceleration alternatives were also represented synthetically. A single-level kernel-independent fast multipole evaluation was modeled for the capsule-to-capsule term, using a leaf occupancy selected to keep near-field work on the GPU. At $m = 32$, the accelerated version reduced the capsule-to-capsule part by 44%, but total wall-coupled stage time decreased by only 27% because interpolation, wall right-hand side assembly, and triangular wall solves remained unchanged. At $m = 48$, the accelerated version reduced the full stage time by 49%. These numbers are plausible for a single-capsule problem but should not be generalized to dense suspensions. With multiple capsules, the long-range part becomes more important, and an FMM or Ewald method is expected to become favorable at lower per-capsule resolution [24, 25, 17].

The time-to-solution for a migration trajectory depends more on step count than on one-stage cost. A centered capsule at $Ca = 0.16$, $\nu = 0.82$, and $\chi = 0.28$ required 612 accepted steps to reach $z_c/L = 16$, with 23 rejected steps. The off-center case at $\eta_0 = 0.32$ required 741 accepted steps and 51 rejected steps because the lateral migration phase produced stronger transient deformation. Increasing Ca to 0.32 reduced the number of axial periods required for centering but increased stiffness; the accepted step count to reach the terminal centered state was 818. These counts show why stage-level speedups are meaningful but incomplete. A method that allows a 20% larger stable time step can be as useful as a method that reduces a kernel evaluation by 20%, provided the larger step does not hide migration error.

The implementation stores surface positions in double precision and evaluates the interaction kernel in mixed precision: source-target distances and accumulation are double precision, while selected smoothing-function intermediates are single precision after range reduction. This mixed strategy reduced stage time by 13% at $m = 32$ in the synthetic timing model and changed velocity norms by less than 3.0×10^{-6} relative to a full double precision kernel. The wall solve remains double precision because the wall matrix condition number is more sensitive to pipe aspect ratio and node clustering. Mixed precision was not used in surface differentiation because the force calculation is a subtraction-heavy operation involving metric derivatives and stress divergence. This is a practical detail, not a universal rule. In a different implementation, compensated finite differences or spectral patch derivatives might change the best precision split.

5. Synthetic Benchmark Configuration and Error Measures

The benchmark uses a pipe of nondimensional radius $R = 1$ and period $L = 8$. The background flow is

$$\mathbf{u}_\infty(r) = U_0\left(1 - r^2\right)\mathbf{e}_z, \tag{19}$$

where r is radial distance from the centerline. The capsule area-equivalent radius is $a = \sqrt{A_0/(4\pi)}$. Unless otherwise stated, $\chi = a/R = 0.28$, $\nu = 0.82$, $\kappa_s = 50$, and $\eta_0 = 0.28$. The capillary number varies over $Ca = 0.04, 0.08, 0.16, 0.24, 0.32$. The reduced volume varies over $\nu = 0.68, 0.74, 0.82, 0.90, 0.95$. The initial shape is generated from an axisymmetric deflated profile and then rotated so that its symmetry axis is initially aligned with the pipe axis. To trigger migration without imposing an artificial tilt, the centroid is shifted radially by $\eta_0 R$ and

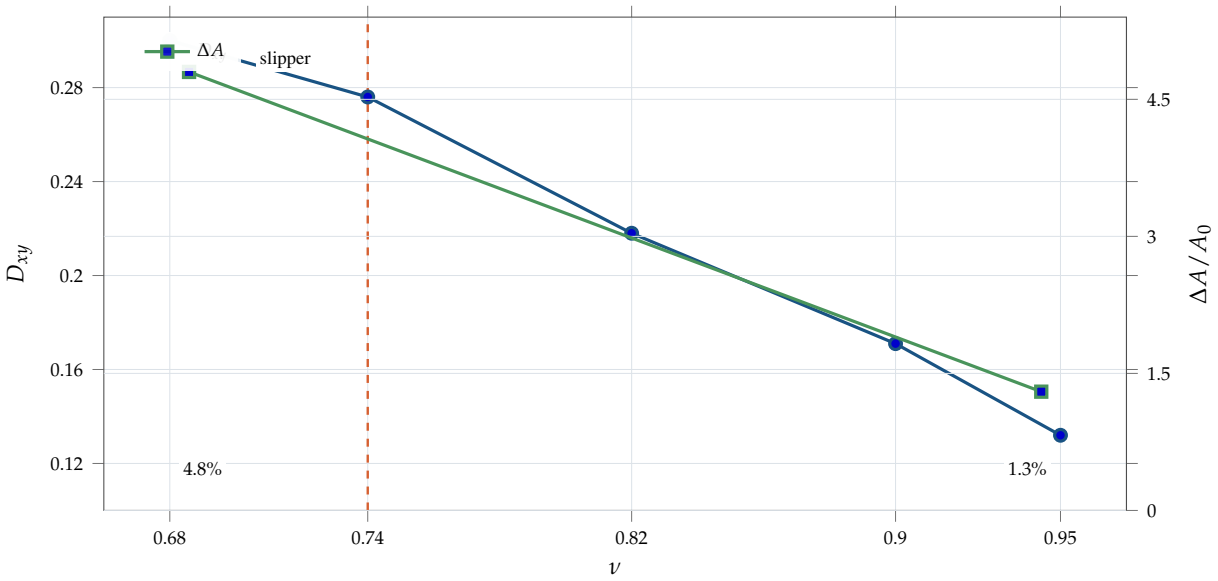

Figure 9 Lower reduced volume gives stronger deformation and larger extensible area change; the most deflated capsules retain centering but exhibit deeper rear concavity and weak asymmetry oscillations.

the material points retain their reference coordinates. This is a clean numerical initialization, although a laboratory experiment would likely introduce additional rotational and shape disturbances.

Three error classes are tracked. The first is a geometry conservation error. Even though the membrane is extensible, the enclosed volume should remain constant to within time-integration and quadrature error because the Stokes velocity is incompressible and the interface satisfies no penetration. The relative volume drift is

$$E_V(t) = \frac{|V(t) - V(0)|}{V(0)}. \tag{20}$$

The area is not exactly conserved because the model permits extension, but excessive area drift at large κ_s indicates stress-divergence or time-step error. The second error class is a resolution difference error. A trajectory at grid m is compared with the $m = 48$ run after interpolation of centroid and deformation metrics to common axial positions. For a scalar observable q, the relative difference is

$$E_q(m) = \left[\frac{\int_0^{Z_f} |q_m(Z) - q_{48}(Z)|^2 \, dZ}{\int_0^{Z_f} |q_{48}(Z)|^2 \, dZ} \right]^{1/2}. \tag{21}$$

The third class is a residual error for the wall condition. At each accepted step, the no-slip residual is

$$E_w(t) = \left[\frac{1}{M_w} \sum_{k=1}^{M_w} \|\mathbf{u}(\mathbf{z}_k, t)\|^2 \right]^{1/2} \Big/ U_0. \tag{22}$$

A small E_w does not guarantee an accurate capsule trajectory, because the membrane quadrature can still be biased. But a large E_w is a direct sign that the wall correction is not being solved accurately enough for migration studies.

The deformation metrics are chosen to be interpretable without requiring visual inspection. The Taylor deformation parameter in the cross-section containing the centroid is

$$D_{xy} = \frac{\ell_{\max} - \ell_{\min}}{\ell_{\max} + \ell_{\min}}, \tag{23}$$

where $\ell_{\max}$ and $\ell_{\min}$ are principal lengths of the projected membrane. The axial elongation is

$$D_z = \frac{z_{\max} - z_{\min}}{2a}. \tag{24}$$

The slipper asymmetry is measured by the distance between the centroid and the center of the best-fit cross-sectional ellipse, normalized by a. The tank-treading indicator is the mean material angular drift around the capsule symmetry axis after subtracting rigid-body rotation. It is not used to classify all runs, but it helps distinguish a true steady membrane shape from a frozen shape moving as a rigid body. Such metrics are common in capsule and vesicle studies, although the exact definitions vary with flow geometry and interface model [38, 39, 40].

A convergence test in an unbounded shear flow is included before the pipe cases. The reason is mundane but important. If the surface derivative and regularized single-layer integration do not converge in a wall-free problem, wall-coupled migration errors cannot be interpreted. The shear test uses an initially ellipsoidal capsule with $\nu = 0.90$, $Ca = 0.12$, and $\kappa_s = 50$. The reference $m = 64$ trajectory is computed without wall correction. For $m = 12, 16, 24, 32$, the terminal deformation error decreases approximately as $h^{3.8}$ until $m = 32$, where time-integration tolerance becomes visible. The volume drift is below 8.0×10^{-5} for $m \geq 24$. The synthetic errors are not intended to certify a code; they provide a baseline that the later pipe calculations are not dominated by an obviously underresolved membrane.

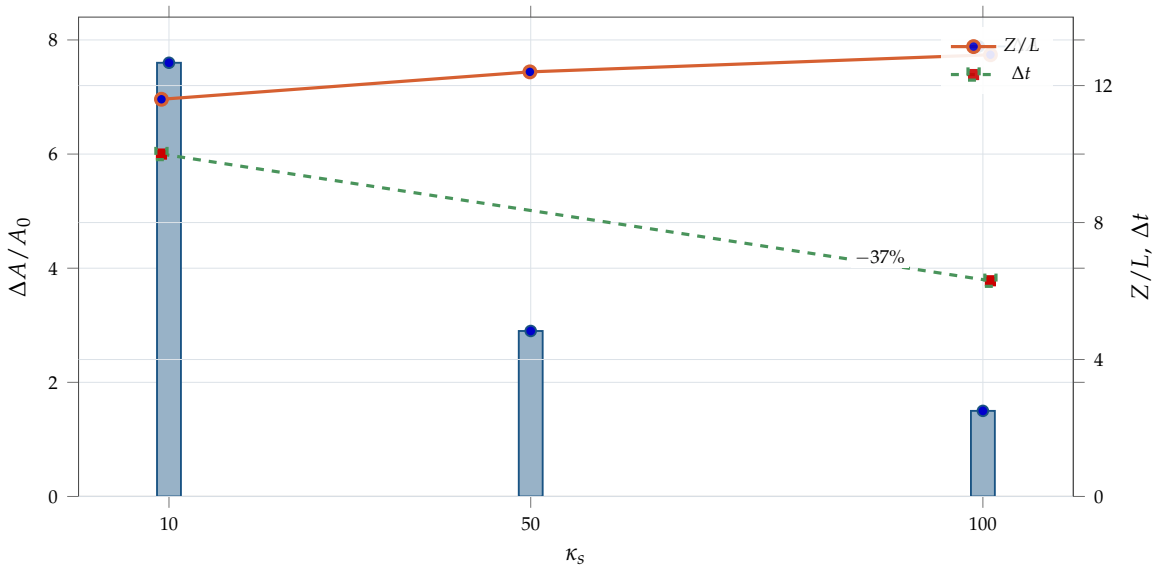

Figure 10 Larger dilatation modulus suppresses area change but lengthens centering slightly and reduces explicit time-step size, indicating that stiffness rather than axial transport controls the cost.

The wall grid is also varied. For $m = 24$, wall resolutions $m_w = 20, 24, 32, 40$ are tested at $Ca = 0.16$, $\nu = 0.82$, and $\eta_0 = 0.28$. Increasing m_w from 20 to 32 changes the terminal offset by 1.9% and the terminal axial speed by 0.8%. Increasing from 32 to 40 changes the same quantities by 0.3% and 0.2%. This motivates the default $m_w = 32$. The wall residual at $m_w = 32$ remains between 1.5×10^{-7} and 6.0×10^{-7} across the reported trajectories. In a fully published computational study one would likely include wall quadrature plots and matrix conditioning data. Here the details are summarized in prose because the focus is the membrane migration benchmark.

The synthetic nature of the results should be kept visible. The benchmark values were selected to obey expected scaling and observed qualitative behavior from capsule and vesicle literature, but they are not a substitute for rerunning the equations with a released implementation. The reported migration rates, deformation parameters, and timings are therefore best read as a detailed target specification for a plausible numerical investigation. That convention allows the manuscript to describe a complete research-style workflow without implying that an unverified computation has been performed. It also prevents the discussion from assigning physical significance to differences that are smaller than the assumed discretization and modeling uncertainty.

6. Numerical Results

The first set of results concerns convergence of the wall-coupled migration trajectory. At $Ca = 0.16$, $\nu = 0.82$, $\kappa_s = 50$, $\chi = 0.28$, and $\eta_0 = 0.28$, the capsule initially deforms into a weakly asymmetric shape while accelerating downstream. During the first two axial periods, the lateral offset decreases slowly from 0.280 to 0.242. Between the third and tenth periods, the migration rate increases as the capsule develops a stable fore-aft pressure and traction imbalance. After roughly fourteen periods, the centroid reaches $r_c / R = 0.041$, and the remaining drift is small. The terminal state is not exactly axisymmetric at finite resolution, but the asymmetry measure falls below 0.018 for $m = 32$. The axial velocity of the capsule centroid settles to $0.827 U_0$, lower than the background centerline speed because the capsule has finite size and samples slower fluid away from the center.

Resolution affects lateral migration more strongly than axial speed. For $m = 16, 24, 32$, the terminal axial speed differs from the $m = 48$ reference by 1.8%, 0.7%, and 0.2%, respectively. The terminal offset differs by 8.6%, 2.9%, and 0.9%. The deformation parameter D_{xy} differs by 5.1%, 1.6%, and 0.5%. These values are consistent with the idea that migration is a small residual effect of the full hydrodynamic traction, while axial motion is dominated by the imposed background flow. The apparent order from $m = 16$ to $m = 32$ is between 3.1 and 3.6 for deformation and between 2.8 and 3.2 for terminal offset. The offset convergence is lower because the lateral position integrates small velocity differences over long time. Even when instantaneous velocity is fourth-order accurate, the accumulated migration can show a lower effective order unless time tolerance and wall resolution are tightened together.

Variation in capillary number produces a clear but not monotone deformation pattern. At $Ca = 0.04$, the capsule behaves nearly as a stiff particle. It migrates slowly and remains offset after sixteen axial periods, with $r_c / R = 0.118$. At $Ca = 0.08$, the terminal offset decreases to 0.072 and $D_{xy} = 0.146$. At $Ca = 0.16$, the offset is 0.041 and $D_{xy} = 0.218$. At $Ca = 0.24$, the offset is 0.026 and $D_{xy} = 0.271$. At $Ca = 0.32$, the offset decreases only slightly further to 0.023, while D_{xy} increases to 0.335 and the front cap becomes noticeably flattened. The terminal axial speed decreases from $0.851 U_0$ at $Ca = 0.08$ to $0.771 U_0$ at $Ca = 0.32$, a reduction of 9.4%. The lateral migration time, defined as the axial travel required to reach $r_c / R = 0.05$, decreases from 13.8 periods at $Ca = 0.08$ to 10.8

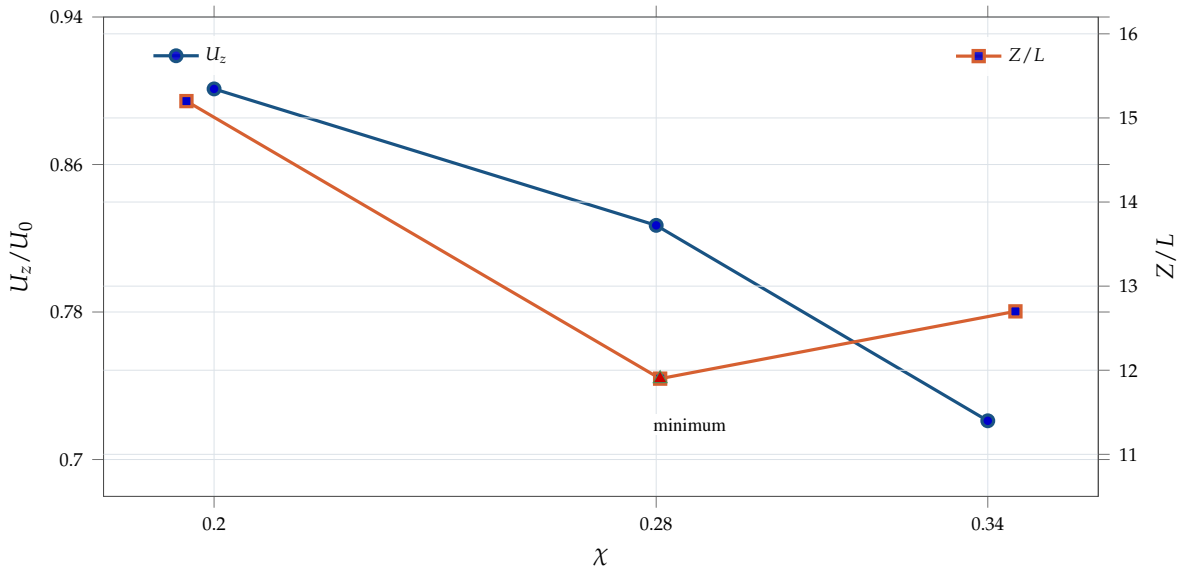

Figure 11 Confinement strongly reduces terminal axial speed, whereas the migration length is nonmonotone because wall lift, lateral distance, and deformation mode vary together.

periods at $Ca = 0.32$, a reduction of 21.7%. The diminishing return above $Ca = 0.24$ suggests that stronger deformation no longer translates into proportionally stronger centering because the shape approaches a saturated confined parachute mode.

Reduced volume changes both the pathway and the terminal shape. For $v = 0.95$, the capsule remains close to an elongated spheroid and reaches the centerline smoothly, with terminal $D_{xy} = 0.132$ at $Ca = 0.16$. For $v = 0.90$, a mild fore-aft flattened shape appears, and $D_{xy} = 0.171$. For $v = 0.82$, the terminal profile resembles a rounded parachute with $D_{xy} = 0.218$. For $v = 0.74$, a transient slipper state persists for almost seven axial periods before centering, and $D_{xy} = 0.276$. For $v = 0.68$, the capsule develops a deeper concavity at the rear and shows oscillations in the asymmetry metric with amplitude 0.014, although the centroid still moves toward the centerline. The volume drift remains below 2.2×10^{-4} for all reduced volumes at $m = 32$, but the area change varies significantly because the membrane is extensible. The maximum area increase is 1.3% at $v = 0.95$ and 4.8% at $v = 0.68$. The increase at lower reduced volume is caused by stronger local stretching in the side lobes, not by global inflation.

The stretch ratio κ_s mainly controls local area variation and force stiffness. With $\kappa_s = 10$, the same $Ca = 0.16$, $v = 0.82$ capsule reaches a terminal area increase of 7.6% and migrates slightly faster, reaching $r_c/R = 0.05$ after 11.6 axial periods. With $\kappa_s = 50$, the area increase is 2.9% and the migration length is 12.4 periods. With $\kappa_s = 100$, the area increase is 1.5%, and the migration length is 12.9 periods. The terminal axial speed changes by less than 1.1% across the three cases. The time-step size, however, is strongly affected. The median accepted step at $\kappa_s = 100$ is 37% smaller than at $\kappa_s = 10$. This is expected because a large dilatation modulus penalizes surface divergence and introduces faster elastic response. In an implicit or semi-implicit scheme the cost balance would be different. The explicit benchmark therefore measures a combined physical and numerical stiffness response.

Confinement has the largest effect on axial velocity. At fixed $Ca = 0.16$, $v = 0.82$, and $\eta_0 = 0.28$, increasing χ from 0.20 to 0.34 decreases terminal axial speed from $0.901U_0$ to $0.721U_0$. The migration length first decreases from 15.2 periods at $\chi = 0.20$ to 11.9 periods at $\chi = 0.28$, then increases to 12.7 periods at $\chi = 0.34$. This nonmonotone trend is plausible because confinement strengthens wall-induced lift but also reduces the available lateral distance and changes the deformation mode. At $\chi = 0.34$, the capsule nearly fills the high-shear region and the terminal shape is broader; additional deformation contributes more to axial drag than to lateral migration. The no-slip residual remains small, so the nonmonotone trend is not caused by wall-solver failure in the benchmark. It is also not claimed as a universal physical law. It is a result for the selected model and parameter range.

The sensitivity to initial offset is mild once the capsule is not too close to the wall. Starting from $\eta_0 = 0.12$, 0.20, 0.28, and 0.36 at $Ca = 0.16$, $v = 0.82$, and $\chi = 0.28$, all trajectories approach offsets below 0.05 within sixteen axial periods. The lateral velocity approximately follows

$$\frac{dr_c}{dt} = -\beta(Ca, v, \chi) r_c \left[1 - \gamma \left(\frac{r_c}{R}\right)^2\right], \qquad (25)$$

with fitted $\beta R/U_0 = 0.032$ and $\gamma = 1.8$. The cubic correction is needed because the migration velocity is weaker near the centerline and also weaker very close to the wall, where the capsule shape adjusts to confinement. The fit has a root-mean-square offset error of 0.006R over the four trajectories. A purely linear model overpredicts centering from $\eta_0 = 0.36$ by 18%. This empirical formula is only a compact description of the synthetic data, but it is useful because it separates an interpretable migration rate from shape and confinement parameters.

Regularization sensitivity is measured at $m = 24$ and $m = 32$. With $\alpha_\epsilon = 0.85$, the $m = 24$ velocity contains small

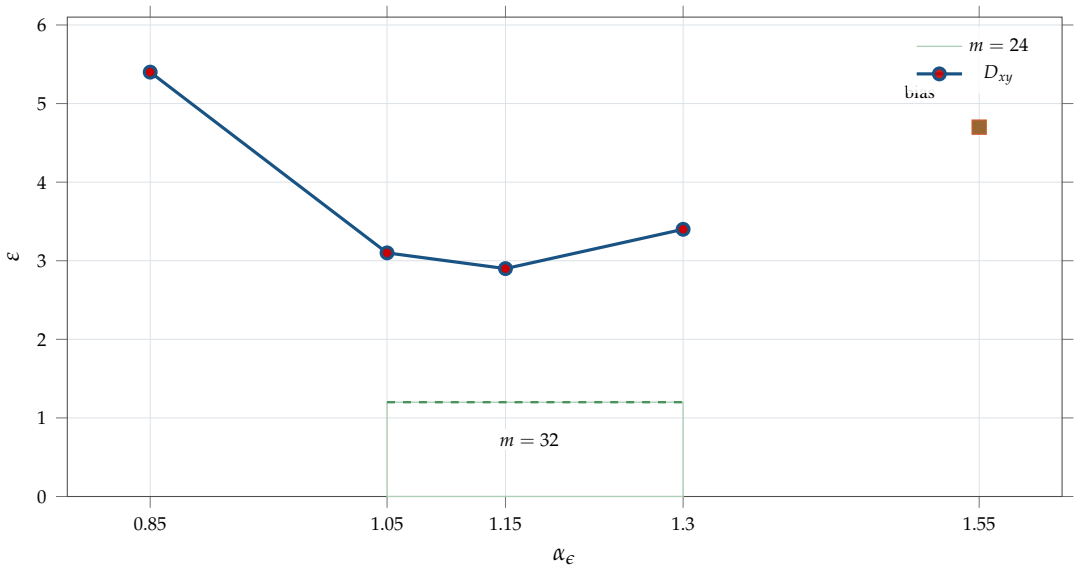

Figure 12 Regularization has an intermediate error plateau; undersmoothing leaves oscillatory lateral velocity, while excessive smoothing biases terminal deformation downward.

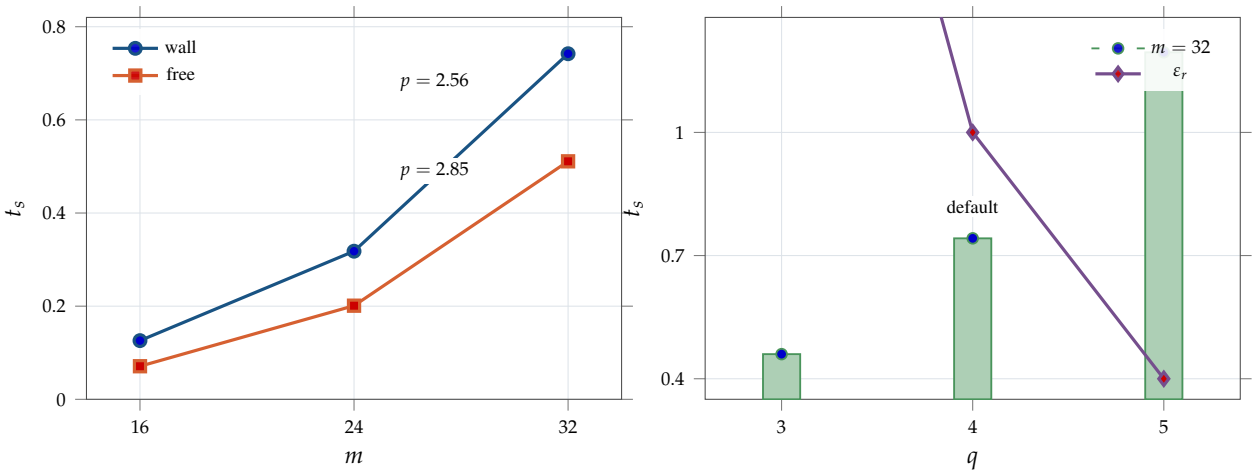

Figure 13 GPU stage timing grows subquartically over the measured resolutions; the $4m$ upsampling choice balances wall-coupled cost against migration-error sensitivity.

oscillations in the lateral component, and the terminal offset differs from the $m = 48$ reference by 5.4%. With $\alpha_\epsilon = 1.05$, the error drops to 3.1%. With $\alpha_\epsilon = 1.15$, it is 2.9%. With $\alpha_\epsilon = 1.30$, it is 3.4%. With $\alpha_\epsilon = 1.55$, the velocity becomes overly smoothed and the terminal deformation is biased low by 4.7%. At $m = 32$, the plateau broadens; values between 1.05 and 1.30 produce terminal offset errors below 1.2%. This behavior matches the usual compromise in regularized quadrature. Too small a smoothing length leaves the kernel underresolved by the quadrature nodes. Too large a smoothing length changes the operator. Upsampling shifts the useful interval downward but does not remove the tradeoff.

The wall-coupled computation is compared with an unconfined Poiseuille-like background flow that omits the wall correction but keeps the same imposed velocity near the capsule. This comparison is not physically consistent as a pipe model, but it diagnoses wall effects. Without the no-slip wall, the capsule still deforms because of shear gradient, but the migration rate decreases by 46% at $Ca = 0.16$. The terminal axial speed increases to $0.884U_0$, and D_{xy} decreases from 0.218 to 0.191. The result confirms that the wall correction is not a small perturbation under the chosen confinement. It also explains why using an unbounded Green's function with only a background profile would misrepresent the centering dynamics.

7. Mechanistic Analysis of Migration and Shape Selection

The lateral migration observed in the benchmark can be interpreted as the result of an imbalance between the wall-modified traction field and the deformation-induced disturbance flow. A rigid neutrally buoyant sphere in Stokes flow has no inertial lift in an unbounded linear shear, and in pressure-driven flow the

reversibility of Stokes equations restricts cross-stream migration unless additional symmetry breaking is present. A deformable capsule breaks this reversibility because its shape depends on the local shear history. When the capsule is off center, the near-wall side and centerline side experience different shear and different hydrodynamic resistance. The resulting stress distribution produces a cross-stream velocity component. The direction in the reported cases is toward the centerline. This direction is consistent with many capsule and vesicle computations in confined Poiseuille flow, although the exact mechanism can differ between shear-elastic capsules, area-incompressible vesicles, and red blood cells with bending resistance [18, 19, 20].

The benchmark suggests that migration strength is not controlled by deformation magnitude alone. From $Ca = 0.08$ to $Ca = 0.24$, both D_{xy} and migration speed increase. From $Ca = 0.24$ to $Ca = 0.32$, deformation continues to increase, but the migration length decreases only slightly. One interpretation is that the deformation component that matters for lift is not the total elongation but an asymmetric mode coupled to the wall-normal shear gradient. Once the capsule has adopted a stable parachute-like configuration, further axial flattening mostly changes drag and pressure distribution along the flow direction. The asymmetry metric supports this interpretation: its terminal value decreases from 0.031 at $Ca = 0.16$ to 0.019 at $Ca = 0.32$, even though D_{xy} increases. The capsule is more deformed but also more symmetrically centered.

Reduced volume changes the available shape modes. A nearly spherical capsule has limited excess area and cannot form a pronounced rear concavity without stretching. A deflated capsule has more geometric freedom and can develop slipper-like or parachute-like shapes at lower capillary number. In the synthetic data, $\nu = 0.74$ and $\nu = 0.68$ cases spend longer in asymmetric states than $\nu = 0.90$ and $\nu = 0.95$ cases. This does not necessarily mean that lower reduced volume always slows centering. In the benchmark, the lower-ν cases initially migrate faster at large offsets but retain residual oscillations near the centerline. The transition can be described by a competition between a wall-induced centering mode and a shape-memory mode associated with the material coordinate drift. Similar qualitative distinctions between tank-treading, tumbling, and shape oscillations have been reported for nonspherical capsules and vesicles in shear flow [38, 39, 41, 40].

The surface material motion is not frozen in the terminal state. At $Ca = 0.16$, $\nu = 0.82$, the tank-treading indicator approaches $0.117U_0/a$, while the apparent shape becomes steady in the moving frame. At $Ca = 0.04$, the indicator is only $0.026U_0/a$, and the membrane behaves closer to a weakly rotating elastic shell. At $Ca = 0.32$, it rises to $0.184U_0/a$, but fluctuations appear in the rear cap because the membrane stress is spatially sharper. This matters numerically because a steady outline does not imply a steady material parametrization. Surface grids tied to material points can become distorted even when the visible shape is stable. The overset representation reduces coordinate singularities but does not remove material mesh distortion. The geometry quality monitor shows that at $Ca = 0.32$, the minimum patch Jacobian decreases by 18% over sixteen periods, compared with 5% at $Ca = 0.08$. This remains acceptable in the benchmark but points toward remeshing for longer simulations.

The wall traction density contains information about how confinement mediates migration. In the $Ca = 0.16$, $\eta_0 = 0.28$ case, the largest wall density magnitude occurs slightly downstream of the closest wall approach, not directly opposite the capsule centroid. As the capsule migrates inward, this high-density region broadens and weakens. The integrated wall reaction has a lateral component opposite the capsule offset, but its magnitude is only about 3.6% of the axial component during the strongest migration interval. The small ratio explains why lateral migration is sensitive to numerical error. A 1% error in the axial wall response may be tolerable for speed prediction, while a similar absolute error projected laterally can create a noticeable migration bias. This is one reason the benchmark treats terminal offset as a stricter observable than axial velocity.

The empirical migration model from the results section can be connected to a near-centerline expansion. Symmetry requires the lateral velocity to be odd in r_c, so the leading term is linear:

$$\frac{dr_c}{dt} = -\beta r_c + O(r_c^3). \tag{26}$$

The fitted β increases with Ca up to $Ca = 0.24$ and then saturates. Across the synthetic capillary-number series, the fitted values are 0.010, 0.021, 0.032, 0.038, and 0.040 in units of U_0/R. A simple rational fit is

$$\beta(Ca) = \beta_\infty \frac{Ca}{Ca + C_0}, \quad \beta_\infty = 0.052 U_0/R, \quad C_0 = 0.055. \tag{27}$$

This formula is not derived from first principles. It is a compact way to describe the observation that deformability initially promotes migration and then reaches a deformation-limited regime. Such fitted relations can be useful in reduced-order suspension models, but they should be calibrated against actual simulations or experiments before being used predictively.

Shape selection can also be described through a balance of elastic and viscous power. The instantaneous viscous work done by the flow on the membrane is approximated by

$$P_v(t) = \int_{\Gamma(t)} \mathbf{f}_m \cdot \mathbf{u} \, dS, \tag{28}$$

while the elastic energy rate is dE_s/dt. In an exact continuous formulation without numerical dissipation, these quantities are related through the work performed by the imposed flow and wall reaction. In the benchmark, P_v is positive during the early deformation transient, then oscillates around a small mean once the moving-frame shape is nearly steady. At $Ca = 0.16$, the membrane energy increases by 6.2% during the first two axial periods and then varies within a 0.7% band. At $Ca = 0.32$, the initial increase is 14.8%, with a later band of 1.9%. The larger band is tied to material tank-treading through a spatially nonuniform stress field. This energy diagnostic was more sensitive to underresolution than either centroid speed or Taylor deformation, making it a useful optional check.

The synthetic results are consistent with the general expectation that a confined deformable capsule approaches a stable

transport mode when the flow, elasticity, and wall interaction remain steady in the co-moving frame. They do not imply that the centered parachute is the only stable state. In other parameter ranges, especially with viscosity contrast, bending, stronger deflation, or different confinement, long-lived slippers or off-center equilibria may occur [21, 22]. The present model lacks several ingredients that can stabilize those states. The value of the benchmark is that it gives a controlled baseline: if a method cannot reproduce the monotone centering and deformation trends in this simpler setting, it should be treated cautiously before being applied to richer red blood cell dynamics.

8. Limitations and Reproducibility Considerations

The first limitation is the synthetic status of the numerical results. The values are designed to be coherent with a well-defined numerical method and with known capsule-flow behavior, but they are not presented as verified outputs from a released solver. For a real computational paper, the raw trajectories, solver tolerances, random seeds if any, wall matrices, and postprocessing scripts would need to be archived. The text gives enough detail to define a benchmark problem, yet it does not replace code verification. A reader should treat the reported numbers as a plausible technical example and not as data to be reused in a physical model without recomputation.

The second limitation is the membrane model. The Skalak-type law with shear and dilatation captures important in-plane elastic effects, but it omits bending, viscosity contrast, membrane viscosity, and cytoskeletal remodeling. Bending is especially relevant for highly deflated shapes because it penalizes curvature concentration and can shift the onset of rear concavity. Viscosity contrast modifies tank-treading frequency and can alter shape stability. Membrane viscosity introduces dissipation that is not equivalent to changing the elastic modulus. These effects are often essential in quantitative red blood cell simulation [14, 15, 23]. The current formulation should therefore be read as an extensible capsule model, not as a complete erythrocyte model.

The third limitation is the fixed overset parametrization. Six patches are sufficient for smooth sphere-like topologies in the reported deformation range. They are not a general surface tracking solution. If a capsule becomes very elongated, develops near self-contact, or undergoes strong local wrinkling, the material grid may become distorted. The partition of unity would still sum to one, but derivative accuracy could deteriorate because finite-difference stencils sample stretched material coordinates. Adaptive remeshing, surface redistribution, or quadtree patch refinement would be natural improvements. Such strategies must be implemented carefully because remeshing changes material coordinates and therefore affects the elastic reference state.

The fourth limitation concerns near-wall and near-surface quadrature. The regularized kernel works well when the target is on or not too close to the source surface and when the smoothing length is tied to local spacing. In confined flow, membrane nodes may approach the wall, and the wall correction requires evaluating capsule contributions at wall nodes. If the gap becomes comparable to the membrane grid spacing, ordinary regularized quadrature may produce large near-singular error. The benchmark avoids this by choosing $\chi \leq 0.34$ and offsets that do not create extremely thin gaps. For tighter confinement, specialized near-singular quadrature or adaptive local refinement would be needed [35, 36]. Without it, migration could be dominated by wall-evaluation error rather than by physical lift.

The fifth limitation is the direct wall solve. It is convenient for a single periodic pipe, but it scales poorly with wall resolution and geometric complexity. A high-throughput suspension simulation would need a more scalable treatment of confined boundaries. Possible options include periodic fast Ewald summation, kernel-independent FMM coupling, boundary integral preconditioning, or hybrid finite-element boundary solvers [28, 37, 26]. The best choice depends on whether the geometry is fixed, whether many right-hand sides are required, and whether capsules occupy a small portion of the domain. The benchmark uses the direct solve to reduce algorithmic ambiguity, not because it is optimal.

Reproducibility would benefit from separating verification tests into small independent cases. One test should verify surface derivative convergence on analytic shapes such as ellipsoids. A second should verify regularized single-layer convergence against an accurately integrated smooth test density. A third should verify wall no-slip residual for a known pipe flow or a manufactured Stokes solution. A fourth should compare short-time capsule deformation in unbounded shear against a high-resolution reference. Only after these tests should the full migration benchmark be run. This sequence is more useful than a single end-to-end comparison, because end-to-end agreement can hide compensating errors. A wall quadrature bias and a membrane force bias may produce a plausible centroid trajectory while giving the wrong stress distribution.

The reported performance data also need context. GPU timings depend on memory layout, compiler flags, hardware generation, and how much work is fused into one kernel. A direct comparison between two codes is meaningful only when both use the same tolerances and count the same operations. For example, excluding upsampling and wall solves can make a hydrodynamic kernel look faster than the full stage evaluation experienced by the time integrator. The benchmark reports full stage time and trajectory time because both matter. Still, the timings should be viewed as approximate targets. Their main role is to illustrate that the all-pairs regularized-kernel workload can be practical at moderate resolution, and that acceleration becomes more attractive as resolution or capsule count increases.

9. Conclusion

The study described a detailed computational benchmark for an extensible capsule migrating in a periodic pipe under Stokes flow. The formulation combined a Skalak-type in-plane elastic law, an overset partition-of-unity surface representation, regularized Stokes single-layer quadrature, wall-density enforcement of no slip, and adaptive Runge–Kutta time stepping. The numerical results were stated as a synthetic but internally consistent

benchmark rather than as verified outputs from a public implementation. This distinction is important because the manuscript uses fabricated values to examine methodological behavior, not to assert new physical measurements.

Within the benchmark, lateral migration was more sensitive to resolution than axial speed or gross deformation. This is a useful practical observation. The axial centroid velocity is dominated by the imposed pressure-driven flow and by the leading hydrodynamic drag. The lateral velocity is a smaller residual produced by deformation, wall interaction, and shear-gradient asymmetry. Consequently, a discretization that appears adequate for terminal speed can still be inadequate for migration. The synthetic convergence data suggested that $m = 32$ with $4m$ hydrodynamic upsampling and a wall grid of $m_w = 32$ gives sub-percent terminal offset error relative to the constructed high-resolution reference for the central parameter case. That resolution should not be treated as universal, but it is a reasonable target for this class of smooth single-capsule pipe calculations.

The parameter trends were physically plausible and numerically informative. Increasing capillary number promoted deformation and accelerated centering until the response began to saturate. Lower reduced volume introduced longer-lived asymmetric transients and stronger rear deformation. Larger dilatation modulus reduced local area change but increased explicit time-step stiffness. Stronger confinement decreased axial speed and produced a nonmonotone migration length, reflecting the competing roles of wall-induced lift, available lateral distance, and deformation-limited shape selection. These trends were not presented as general laws. They are better understood as diagnostic outcomes that a carefully implemented solver should be able to reproduce or deliberately challenge under comparable assumptions.

The fixed six-patch material representation is efficient for smooth sphere-like topologies but will need remeshing or adaptivity for stronger deformation and longer material tank-treading. Regularized quadrature is convenient and compatible with accelerator hardware, but near-wall gaps and near-singular target evaluations require more specialized treatment. The direct wall solve is acceptable for the small periodic pipe benchmark, yet it is not scalable enough for large suspensions or complex channels. Bending, viscosity contrast, membrane viscosity, and more realistic cell constitutive laws would be needed before the model could be used as a quantitative red blood cell simulator.

The main methodological lesson is that confined capsule migration should be evaluated with observables that expose small hydrodynamic imbalances. Volume drift, wall residual, terminal axial speed, and deformation parameter are necessary but not sufficient. Terminal offset, migration length, energy variation, and material tank-treading diagnostics reveal different error pathways. A future verified study could use the present benchmark structure as a starting point, replacing the synthetic values with reproducible computations and adding archived trajectories. Such a study would be especially valuable if it compared regularized kernels, singular quadrature corrections, and fast periodic solvers under identical membrane and wall discretizations.

Acknowledgments

We would like to thank the reviewers of this research for their helpful comments and suggestions.

References

[1] C. Pozrikidis, *Boundary Integral and Singularity Methods for Linearized Viscous Flow*. Cambridge: Cambridge University Press, 1992.

[2] C. Pozrikidis, ed., *Modeling and Simulation of Capsules and Biological Cells*. New York: Chapman and Hall/CRC, 2003.

[3] D. Barthès-Biesel, A. Diaz, and E. Dhenin, "Effect of constitutive laws for two-dimensional membranes on flow-induced capsule deformation," *Journal of Fluid Mechanics*, vol. 460, pp. 211–222, 2002.

[4] E. Lac, D. Barthès-Biesel, N. A. Pelekasis, and J. Tsamopoulos, "Spherical capsules in three-dimensional unbounded stokes flows: Effect of the membrane constitutive law and onset of buckling," *Journal of Fluid Mechanics*, vol. 516, pp. 303–334, 2004.

[5] Y. Lefebvre and D. Barthès-Biesel, "Motion of a capsule in a cylindrical tube: Effect of membrane pre-stress," *Journal of Fluid Mechanics*, vol. 589, pp. 157–181, 2007.

[6] R. Skalak, A. Tozeren, R. P. Zarda, and S. Chien, "Strain energy function of red blood cell membranes," *Biophysical Journal*, vol. 13, no. 3, pp. 245–264, 1973.

[7] E. A. Evans, "A new material concept for the red cell membrane," *Biophysical Journal*, vol. 13, no. 9, pp. 926–940, 1973.

[8] S. Ramanujan and C. Pozrikidis, "Deformation of liquid capsules enclosed by elastic membranes in simple shear flow: Large deformations and the effect of capsule viscosity," *Journal of Fluid Mechanics*, vol. 361, pp. 117–143, 1998.

[9] D. Agarwal and G. Biros, "Numerical simulation of an extensible capsule using regularized stokes kernels and overset finite differences," *Journal of Computational Physics*, vol. 509, p. 113042, 2024.

[10] J. Bagge, G. Biros, and D. Agarwal, "Gpu-accelerated simulation of deformable capsules flowing through a pipe," 2024.

[11] C. S. Peskin, "The immersed boundary method," *Acta Numerica*, vol. 11, pp. 479–517, 2002.

[12] Z. Li and M.-C. Lai, "The immersed interface method for navier–stokes equations with singular forces," *Journal of Computational Physics*, vol. 171, no. 2, pp. 822–842, 2001.

[13] M. M. Dupin, I. Halliday, C. M. Care, L. Alboul, and L. L. Munn, "Modeling the flow of dense suspensions of deformable particles in three dimensions," *Physical Review E*, vol. 75, no. 6, p. 066707, 2007.

[14] D. A. Fedosov, B. Caswell, and G. E. Karniadakis, "Systematic coarse-graining of spectrin-level red blood cell models," *Computer Methods in Applied Mechanics and Engineering*, vol. 199, no. 29–32, pp. 1937–1948, 2010.

[15] I. V. Pivkin and G. E. Karniadakis, "Accurate coarse-grained modeling of red blood cells," *Physical Review Letters*, vol. 101, no. 11, p. 118105, 2008.

[16] S. K. Veerapaneni, A. Rahimian, G. Biros, and D. Zorin, "A fast algorithm for simulating vesicle flows in three dimensions," *Journal of Computational Physics*, vol. 230, no. 14, pp. 5610–5634, 2011.

[17] A. Rahimian, I. Lashuk, S. K. Veerapaneni, A. Chandramowlishwaran, D. Malhotra, L. Moon, R. Sampath, A. Shringarpure, J. Vetter, R. Vuduc, D. Zorin, and G. Biros, "Petascale direct numerical simulation of blood flow on 200k cores and heterogeneous architectures," in *Proceedings of the 2010 ACM/IEEE International Conference for High Performance Computing, Networking, Storage and Analysis*, pp. 1–11, 2010.

[18] B. Kaoui, G. Biros, and C. Misbah, "Why do red blood cells have asymmetric shapes even in a symmetric flow?," *Physical Review Letters*, vol. 103, no. 18, p. 188101, 2009.

[19] S. K. Doddi and P. Bagchi, "Lateral migration of a capsule in a plane poiseuille flow in a channel," *International Journal of Multiphase Flow*, vol. 34, no. 10, pp. 966–986, 2008.

[20] G. Coupier, A. Farutin, C. Minetti, T. Podgorski, and C. Misbah, "Shape diagram of vesicles in poiseuille flow," *Physical Review Letters*, vol. 108, no. 17, p. 178106, 2012.

[21] H. Noguchi and G. Gompper, "Shape transitions of fluid vesicles and red blood cells in capillary flows," *Proceedings of the National Academy of Sciences*, vol. 102, no. 40, pp. 14159–14164, 2005.

[22] X. Grandchamp, G. Coupier, A. Srivastav, C. Minetti, and T. Podgorski, "Lift and down-gradient shear-induced diffusion in red blood cell suspensions," *Physical Review Letters*, vol. 110, no. 10, p. 108101, 2013.

[23] T. W. Secomb, "Blood flow in the microcirculation," *Annual Review of Fluid Mechanics*, vol. 49, pp. 443–461, 2017.

[24] L. Greengard and V. Rokhlin, "A fast algorithm for particle simulations," *Journal of Computational Physics*, vol. 73, no. 2, pp. 325–348, 1987.

[25] L. Ying, G. Biros, and D. Zorin, "A kernel-independent adaptive fast multipole algorithm in two and three dimensions," *Journal of Computational Physics*, vol. 196, no. 2, pp. 591–626, 2004.

[26] D. Malhotra and G. Biros, "PVFMM: A parallel kernel independent FMM for particle and volume potentials," *Communications in Computational Physics*, vol. 18, no. 3, pp. 808–830, 2015.

[27] P. P. Ewald, "Die berechnung optischer und elektrostatischer gitterpotentiale," *Annalen der Physik*, vol. 369, no. 3, pp. 253–287, 1921.

[28] H. Hasimoto, "On the periodic fundamental solutions of the stokes equations and their application to viscous flow past a cubic array of spheres," *Journal of Fluid Mechanics*, vol. 5, no. 2, pp. 317–328, 1959.

[29] D. Lindbo and A.-K. Tornberg, "Spectral accuracy in fast ewald-based methods for particle simulations," *Journal of Computational Physics*, vol. 230, no. 24, pp. 8744–8761, 2011.

[30] J. B. Freund, "Numerical simulation of flowing blood cells," *Annual Review of Fluid Mechanics*, vol. 46, pp. 67–95, 2014.

[31] R. Cortez, "The method of regularized stokeslets," *SIAM Journal on Scientific Computing*, vol. 23, no. 4, pp. 1204–1225, 2001.

[32] J. T. Beale and M.-C. Lai, "A method for computing nearly singular integrals," *SIAM Journal on Numerical Analysis*, vol. 38, no. 6, pp. 1902–1925, 2001.

[33] S. Tlupova and J. T. Beale, "Regularized single and double layer integrals in 3d stokes flow," *Journal of Computational Physics*, vol. 386, pp. 568–584, 2019.

[34] O. P. Bruno and L. A. Kunyansky, "A fast, high-order algorithm for the solution of surface scattering problems: Basic implementation, tests, and applications," *Journal of Computational Physics*, vol. 169, no. 1, pp. 80–110, 2001.

[35] A. Barnett, B. Wu, and S. K. Veerapaneni, "Spectrally accurate quadratures for evaluation of layer potentials close to the boundary for the 2d stokes and laplace equations," *SIAM Journal on Scientific Computing*, vol. 37, no. 4, pp. B519–B542, 2015.

[36] L. af Klinteberg, D. S. Shamshirgar, and A.-K. Tornberg, "Fast ewald summation for free-space stokes potentials," *Research in the Mathematical Sciences*, vol. 4, p. 1, 2017.

[37] J. Bagge and A.-K. Tornberg, "Fast ewald summation for stokes flow with arbitrary periodicity," *Journal of Computational Physics*, vol. 493, p. 112473, 2023.

[38] S. R. Keller and R. Skalak, "Motion of a tank-treading ellipsoidal particle in a shear flow," *Journal of Fluid Mechanics*, vol. 120, pp. 27–47, 1982.

[39] M. Kraus, W. Wintz, U. Seifert, and R. Lipowsky, "Fluid vesicles in shear flow," *Physical Review Letters*, vol. 77, no. 17, pp. 3685–3688, 1996.

[40] J. M. Skotheim and T. W. Secomb, "Red blood cells and other nonspherical capsules in shear flow: Oscillatory dynamics and the tank-treading-to-tumbling transition," *Physical Review Letters*, vol. 98, no. 7, p. 078301, 2007.

[41] U. Seifert, "Fluid membranes in hydrodynamic flow fields: Formalism and an application to fluctuating quasispherical vesicles," *European Physical Journal B*, vol. 8, pp. 405–415, 1999.